Building Robust Architectures of Carbon and Metal Oxide Nanocrystals toward High-Performance Anodes for Lithium-Ion Batteries

Xilai Jia,[†] Zheng Chen,[‡] Xia Cui,[‡] Yiting Peng,[‡] Xiaolei Wang,[‡] Ge Wang,[§,*] Fei Wei,[†,*] and Yunfeng Lu[‡,*]

[†]Beijing Key Laboratory of Green Chemical Reaction Engineering and Technology, Department of Chemical Engineering, Tsinghua University, Beijing 100084, People's Republic of China, [‡]Department of Chemical and Biomolecular Engineering, University of California, Los Angeles, California 90095, United States, and [§]School of Materials Science and Engineering, University of Science and Technology Beijing, Beijing 100083, People's Republic of China

ABSTRACT Design and fabrication of effective electrode structure is essential but is still a challenge for current lithium-ion battery technology. Herein we report the design and fabrication of a class of high-performance robust nanocomposites based on iron oxide spheres and carbon nanotubes (CNTs). An efficient aerosol spray process combined with vacuum filtration was used to synthesize such composite architecture, where oxide nanocrystals were assembled into a continuous carbon skeleton and entangled in porous CNT networks. This material architecture offers many critical features that are required for high-performance anodes, including efficient ion transport, high conductivity, and structure durability, therefore enabling an electrode with outstanding lithium storage performance. For example, such an electrode with a thickness of ~35 μm could deliver a specific capacity of 994 mA h g^{-1} (based on total electrode weight) and high recharging rates. This effective strategy can be extended to construct many other composite electrodes for high-performance lithium-ion batteries.

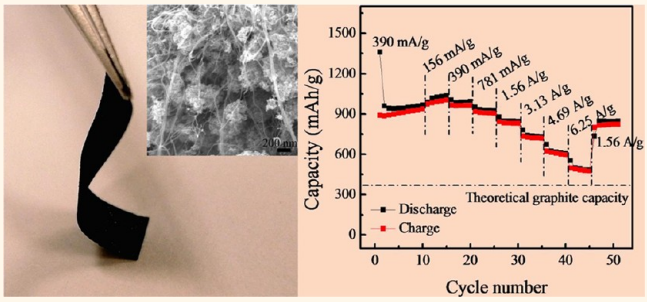

KEYWORDS: lithium-ion battery · flexible electrode · iron oxide · carbon nanotube · aerosol spray

Lithium-ion batteries are commonly used for electronics, electric vehicles, and other applications.[1,2] Despite their broad use, developing better energy storage devices with further improved performance, such as higher energy density and power density, remains as the main theme of the field.[3−5] In this context, transition metal oxides, which possess significantly higher capacities than that of the current commercial anode material (graphite),[6−12] hold great promise toward a high-energy-density anode; however, such promise has been hampered by their poor cycling stability and rate performance.

To address this challenge, it is critically important to design electrodes rooted from their structure and operation principle. Traditionally, electrodes were fabricated from mixtures of active materials, conductive agent (*e.g.*, carbon black), and polymeric binders,[13,14] in which ion transport and electron transport networks were constructed. During the charge/discharge process, electrons and ions are shuffled between the anode and cathode, where electrical energy and chemical energy are transformed reversibly. The rate performance of an electrode is determined by the rate of electron and ion transport, while the cycling stability will be determined by the durability of such transport networks. Recognize that metal oxides generally possess low electrical and ion conductivities, which unavoidably results in the low-rate performance. Moreover, due to the large volume change of oxide materials during the charge/discharge process, as-formed electrical conductive networks (carbon−carbon contacts) may be destroyed easily. Furthermore, due to unfavorable electrochemical reactions, electrically insulated or ion-diffusion-resistant

* Address correspondence to wf-dce@tsinghua.edu.cn, luucla@ucla.edu, gewang@mater.ustb.edu.cn.

Received for review August 2, 2012 and accepted October 9, 2012.

Published online October 09, 2012
10.1021/nn303478e

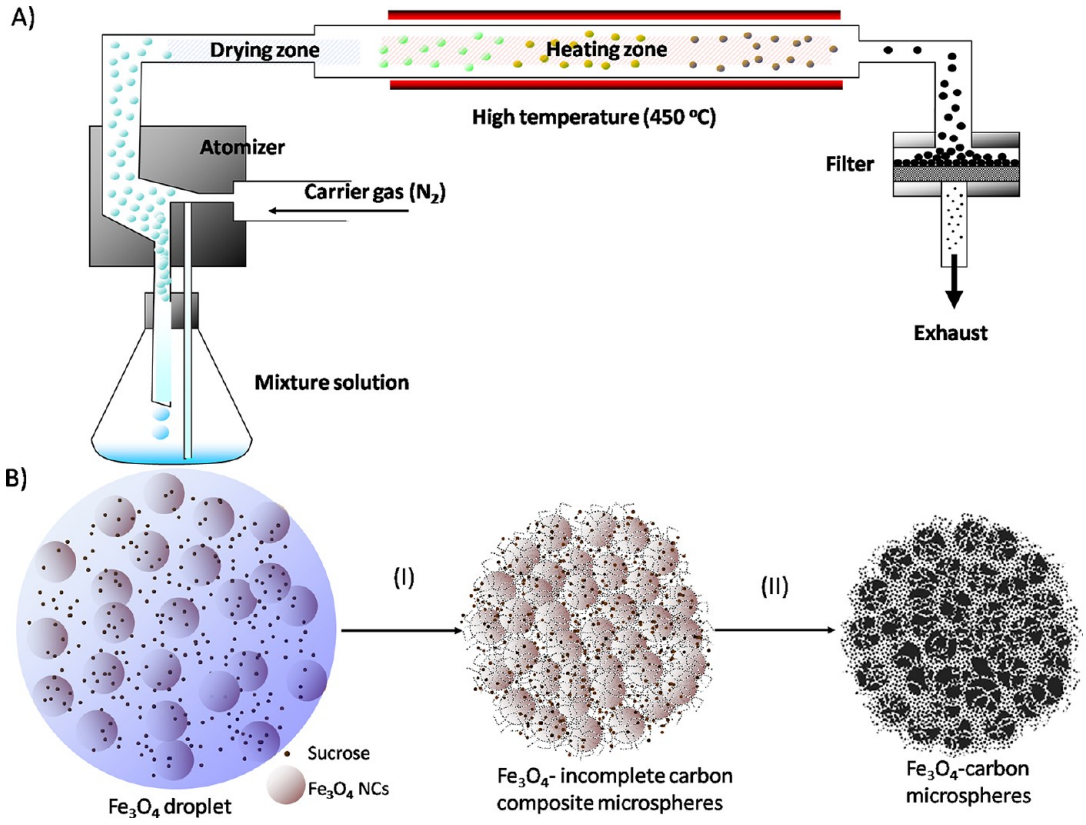

Scheme 1. Synthesis process of Fe_3O_4/carbon nanocomposite particles. (A) Scheme synthesizing Fe_3O_4/carbon composite particles using an aerosol spraying process. (B) Scheme further illustrating the formation of the composite particles. Starting from aerosol droplets containing Fe_3O_4 nanocrystals and sucrose, solvent evaporation followed by sucrose decomposition in the heating zone creates iron oxide composite particles (I); subsequent carbonization process converts the particles into porous Fe_3O_4/carbon composited particles (II).

layers may also be formed on the oxide surface, which further deteriorates effectiveness of the ion and electron transport.

To date, various approaches have been explored to construct more effective and durable ion and electron transport networks. The simplest strategy is to replace the carbon black with carbon nanotubes (CNTs)[7,15,16] or graphene.[17−19] CNTs often exhibit high aspect ratios and excellent conductivity, while graphene exhibits good conductivity and strong $\pi-\pi$ interactions; their uses may improve the rate performance and stability to a certain degree. Coating electrode active materials with thin layers of structure-enforcing materials (*e.g.*, SiO_2 and Al_2O_3) was also explored.[20−22] This was often achieved by chemical vapor deposition (CVD)[20] or atomic layer deposition (ALD)[21,22] methods. Such coatings may effectively stabilize the electrodes without significantly increasing the transport resistance for both ions and electrons. However, such deposition processes require expensive precursors and facilities and are difficult to implement for large-scale production. Coating the active electrode materials with carbon has been another strategy, which is of particular interest for commercial applications. This is generally achieved by mixing oxide particles or their precursors with carbon sources (*e.g.*, glucose) followed by a carbonization process,[13,23] which leads to the formation of isolated oxide particles coated with carbon. Although improved rate performance and stability were often achieved, this process often resulted in low tapping density, particularly for the case of nanosize oxide particles. Overall, despite the great efforts and the success stated above, construction of robust electron and ion conductive networks leading to high-performance anode remains challenging.

Herein, we report the design and fabrication of nanocomposites of iron oxide and carbon with high capacity, excellent rate performance, and high cycling stability. Iron oxide was used as the model system due to its high capacity, nontoxicity, and low cost. As illustrated in Scheme 1, we started with precursor solutions containing Fe_3O_4 nanocrystals (NCs) and sucrose; an aerosol spraying process[24,25] generates droplets containing the precursor (Scheme 1A). Solvent (water) evaporation enriches the NCs and sucrose, enabling the NCs to be assembled into continuous NC networks. Subsequent sintering and carbonization process at 560 °C for 2 h under nitrogen further strengthened the NC networks and coated them with continuous layers of carbon, leading to the formation of robust Fe_3O_4/carbon composite spheres with rough surface morphology (Scheme 1B). Mixing the rough

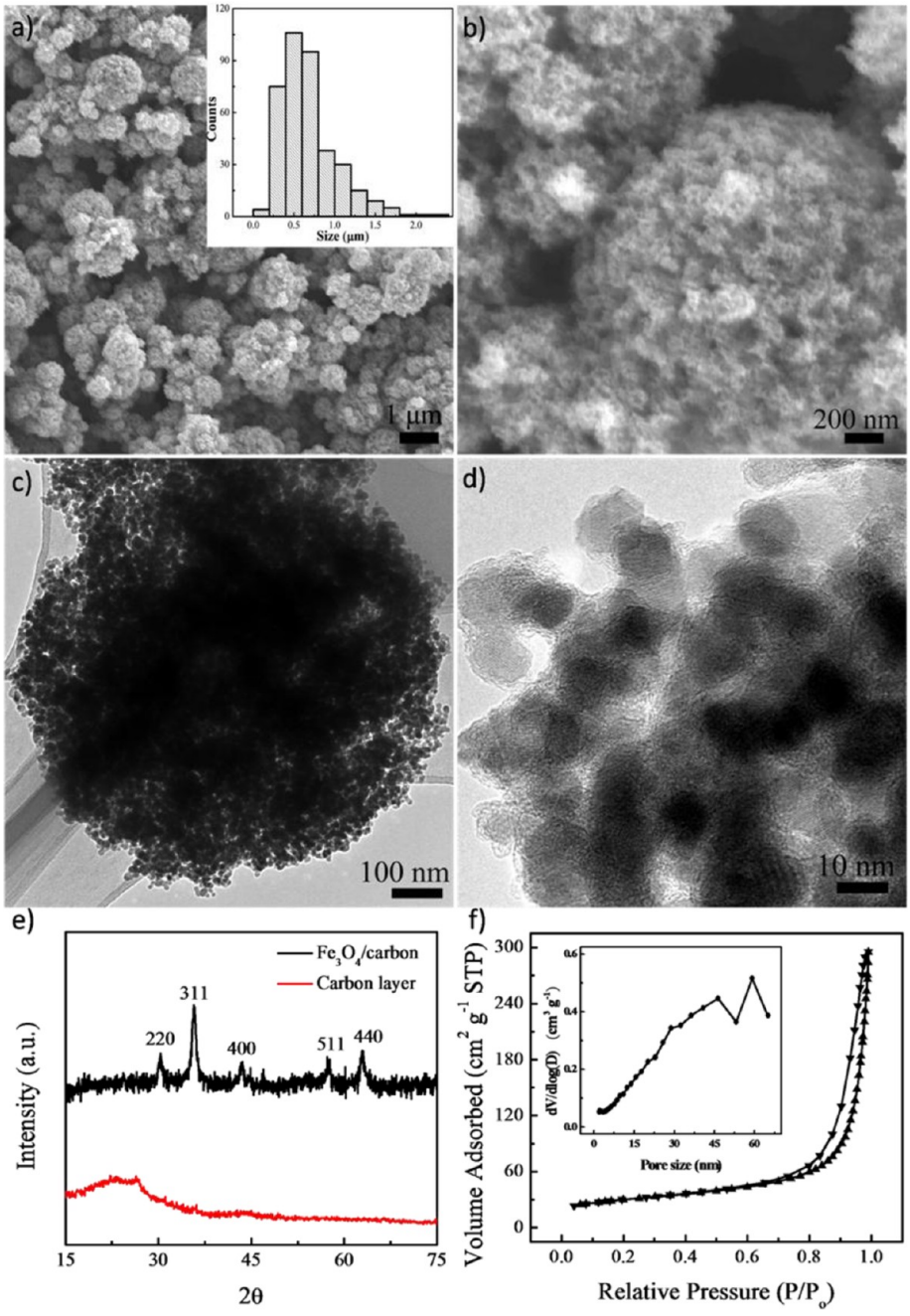

Figure 1. SEM and TEM images of the hierarchically porous Fe_3O_4/carbon composite particles: (a) low-magnification SEM image showing as-produced particles (inset: size distribution of the spheres); (b) high-magnification SEM image showing the particles with rough surface; (c) TEM image of the hierarchically porous oxide clusters; (d) high-magnification TEM image showing the formation of continuous carbon skeleton and Fe_3O_4 nanocrystal networks; (e) XRD patterns of the Fe_3O_4/carbon composite particles and amorphous carbon derived from the composite particles by etching Fe_3O_4 using nitric acid; (f) nitrogen sorption isotherms and pore size distribution (inset) of the porous Fe_3O_4/carbon particles.

surface spheres with carbon nanotubes (CNTs) in solution followed by a filtration process enables the formation of binder-free electrodes,[7,26,27] within which the CNTs and the spheres are highly entangled, forming robust and flexible networks.

This simple composite structure offers many critical features. (1) In the aspect of ion transport, the composite spheres are built from individual NCs, which retain their short lithium diffusion length. As-formed nanocrystalline networks also create three-dimensional (3D) interconnected channels, enabling fast transport of lithium ions. (2) In the aspect of electron transport, the carbon coatings are formed continuously on the entire NC networks, providing effective electron transport. Moreover, the intimate entanglement between the conductive CNT networks and the carbon-coated composite spheres further establishes hierarchical networks for electron transport. (3) In the aspect of structure

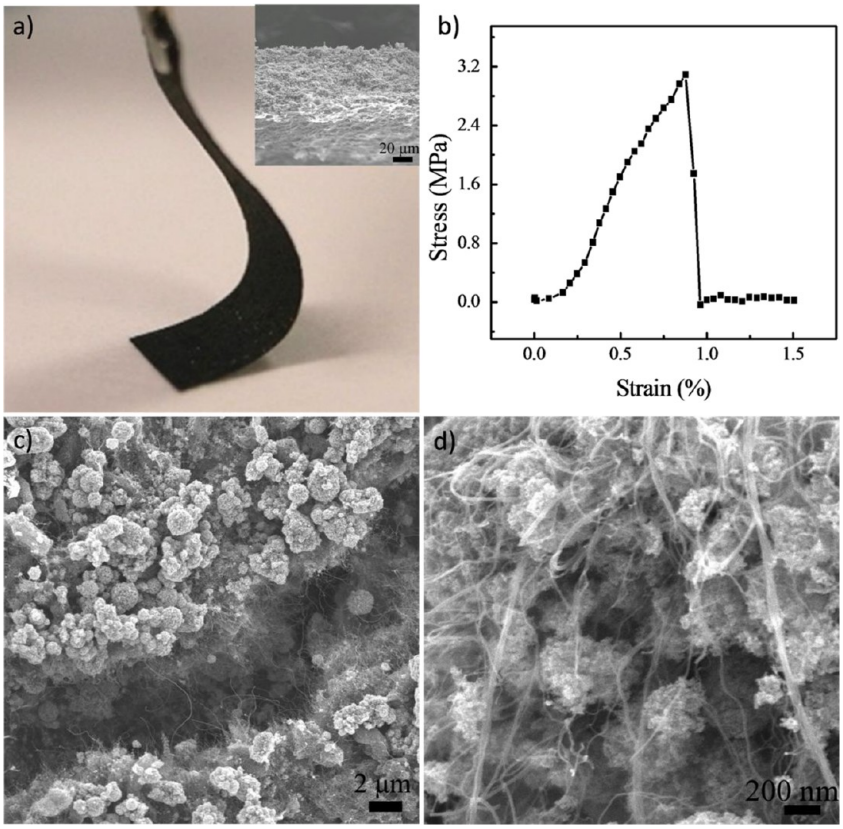

Figure 2. (a) Photograph of a flexible electrode (inset is the cross-section SEM image of the electrode showing its thickness); (b) representative stress−strain curve of the flexible electrode; (c,d) SEM images of a fractured electrode showing an intimate entanglement between the composite particles and the CNT networks.

stability, the composite spheres are constructed from networks of NCs through strong ionic bonding, which ensures the structure robustness. Moreover, the carbon coatings and the elastic CNT networks also mitigate the mechanical stress that may be generated during their charge/discharge process, endowing electrodes with structural durability. It is also important to point out that a spraying process has been broadly used for large-scale production of micrometer-size particles of active materials,[28,29] while Fe_3O_4 and sucrose are abundant and available at low cost. Moreover, mass production of CNTs has also been implemented,[30] which enables the production of CNTs at a price comparable to that of carbon black. Therefore, this work provides a highly effective approach that can be readily scaled up for real application.

RESULTS AND DISCUSSION

The structure and morphology of the composite particles were characterized using electron microscopic techniques and X-ray diffraction (XRD). The low-magnification scanning electron microscopic (SEM) image in Figure 1a shows that as-formed particles exhibit diameters ranging from 0.2 to 1.5 μm (inset in Figure 1a). Higher-magnification SEM image (Figure 1b) reveals that these particles have rough surfaces. A typical particle is observed under transmission electron microscopy (TEM) (Figure 1c); the nanosize Fe_3O_4 crystals are assembled to form cluster networks, with open pores interpenetrating through the clusters. Higher-magnification TEM image (Figure 1d) reveals that all of the Fe_3O_4 NCs are embedded within porous carbon networks with a thickness of around 2−3 nm. It was also found that the size of the NCs within the network is similar to those of the building NCs (4−13 nm in diameter; see Figure S1 in Supporting Information). XRD study reveals that the embedded Fe_3O_4 NCs within the composite exhibit a cubic inverse spinel structure (Figure 1e),[31] and the carbon layer is amorphous. Thermal gravimetric analysis (TGA) shows that the as-formed Fe_3O_4/carbon particles are composed of 86 wt % Fe_3O_4 and 14 wt % carbon (Figure S2). The pore structure of the composite particles was further characterized with nitrogen sorption analysis (Figure 1f). These particles exhibit a high pore volume of 0.45 $cm^3\ g^{-1}$ and a Brunauer−Emmett−Teller (BET) surface area of 103.7 $m^2\ g^{-1}$. Significant nitrogen uptake at a high relative pressure, as well as the absence of significant adsorption−desorption hysteresis, suggests the formation of interconnected porous channels with large pore diameter.

Large-area electrodes with a thickness of 30−70 μm (*ca.* 52 μm, inset in Figure 2a) were obtained from a simple vacuum filtration of a mixture containing Fe_3O_4/carbon particles and CNTs (diameter of 10−20 nm and

length of several tens of micrometers, Figure S3). The high-aspect-ratio CNTs well entangle with the Fe_3O_4/carbon particles, forming flexible free-standing electrodes without adding any polymeric binder. Figure 2a shows a digital photograph of a representative electrode containing 86 wt % composite particles and 14 wt % CNTs. Such highly entangled electrodes show flexibility and good mechanical strength. As shown in the stress−strain curves (Figure 2b), the electrode displays an average tensile strength of 3.1 MPa at a strain of 0.9%. Accordingly, the electrodes possess an average elastic modulus of 340 MPa. Such strong composite electrodes are rarely achieved, though some flexible electrodes have been reported,[32,33] which ensures the electrode structure stability. Figure 2c,d shows the surface and cross-section SEM images of an electrode, where the particles are tightly trapped in the CNT networks. The intimate contacts between the composite particles and the CNTs provide robust electrical conductive pathways, which is critical for high-rate application. Moreover, such composites present a highly flexible architecture that can accommodate the volume change and retain conductive network, providing critical features for high-performance electrodes.

To measure their electrochemical performance, coin cells were fabricated using a lithium disk as the counter electrode and 1.0 M $LiPF_6$ in ethylene carbonate (EC)/diethyl carbonate (DEC) (1:1 by volume) as the electrolyte. Charge storage behavior was first characterized by cyclic voltammetry (CV). Figure 3a shows representative CV curves of the composite electrode. For the first discharge cycle, two well-defined reduction peaks are observed at 1.55 and 0.46 V (*vs* Li/Li^+), respectively. The peak at 1.55 V corresponds to the structure transition induced by lithium intercalation into crystalline Fe_3O_4 ($Fe_3O_4 + xLi^+ + xe^- \rightarrow Li_xFe_3O_4$). The peak at 0.46 V is attributed to the further reduction of $Li_xFe_3O_4$ to Fe(0) by conversion reaction [$Li_xFe_3O_4 + (8 - x)Li^+ + (8 - x)e^- \rightarrow 4Li_2O + 3Fe$], which has been discussed in detail in previous works.[7,12,34] Note that the lithium intercalation at a low voltage below 1 V also causes the formation of a surface electrolyte interphase (SEI), which results in irreversible capacity loss. In the subsequent cycles, redox reactions of lithium insertion/extraction are highly reversible, where the cathodic lithium insertion mainly occurs at 0.65 V and the anodic lithium extraction occurs at 1.9 V due the structure of Fe_3O_4 in the first cycle. Figure 3b shows the charge/discharge curves of the electrode at a current density of 200 mA g^{-1} from 3.0 to 0.005 V. A potential plateau appears at ~0.5 V during the first discharge process, which is in good agreement with the CV results. The initial charge and discharge capacities are 1148 and 821 mAh g^{-1}, respectively, corresponding to an irreversible capacity loss of ~30%, which is commonly observed for oxide-based anodes.[7,13,35] The charge/discharge efficiency approaches 100% in the following cycles, which suggests a facile lithium insertion/extraction associated with efficient transport of ions and electrons in the electrodes.

Figure 3c,d shows the rate performance of the composite electrodes (thickness of ~35 μm) at different current densities (from 156 mA g^{-1} to 6.25 A g^{-1}). At a charge/discharge rate of 156 mA g^{-1} (corresponding to ~0.2 C), a reversible capacity of 994 mAh g^{-1} was realized based on the total weight of the electrode, suggesting a high reversible capacity of the electrodes. When current density is increased to 1.56 A g^{-1}, the electrode can deliver a reversible capacity of ~830 mAh g^{-1}. Even at very high rates, such as 4.69 and 6.25 A g^{-1}, the electrode retains a capacity of 604 and 482 mAh g^{-1}, respectively, which is far exceeding the theoretical capacity of graphite at low rate (~350 mAh g^{-1}). The charge/discharge curves still maintain kinetics feature at high rates when compared to slow rates, indicating a facile charge transport process. Remarkably, when the current density returned to 1.56 A g^{-1} after cycling at different rates, a capacity of 823 mAh g^{-1} was recovered in another 50 cycles (Figure S4).

To further demonstrate the advantages of using the spherical Fe_3O_4/carbon composite for lithium storage, control electrodes with similar thickness and composition were also fabricated by directly mixing the Fe_3O_4 NCs with CNTs based on an identical fabrication method (Figure S5). Apparently, the Fe_3O_4 NCs show much poorer rate capability and stability and cannot bear large current density due to the inefficient electron transport (*e.g.*, capacity was less than ~300 mAh g^{-1} at a current density of 1.56 A g^{-1}). On the other hand, the Fe_3O_4/carbon composite spheres were also mixed with CNTs and PVDF binder, which were then coated on current collectors to prepare conventional electrodes. Figure S6 reveals that such traditional electrodes can reach comparable capacity at low current density; however, charge storage capacity at high rates was not comparable to the flexible, binder-free composite electrodes. The polymeric binders may account for the rate loss due to its insulating nature. Furthermore, polymer binder (10% in total weight) also compromises overall storage capability. Therefore, building binder-free, robust architecture from spherical Fe_3O_4/carbon composite and CNT is critical to achieve the high performance for the composite electrodes.

It should be noted that similar high-rate performance has been achieved in thin film electrodes (less than 10 μm) before[7,36] but has never been reported in electrodes with a thickness of tens of micrometers, in which significantly increased transport resistance and structure instability were often observed. Nevertheless, using such CNT-based composites, we can readily realize such high performance in thick electrodes. Figure 3e reveals that the rate capability of such a thick electrode is higher

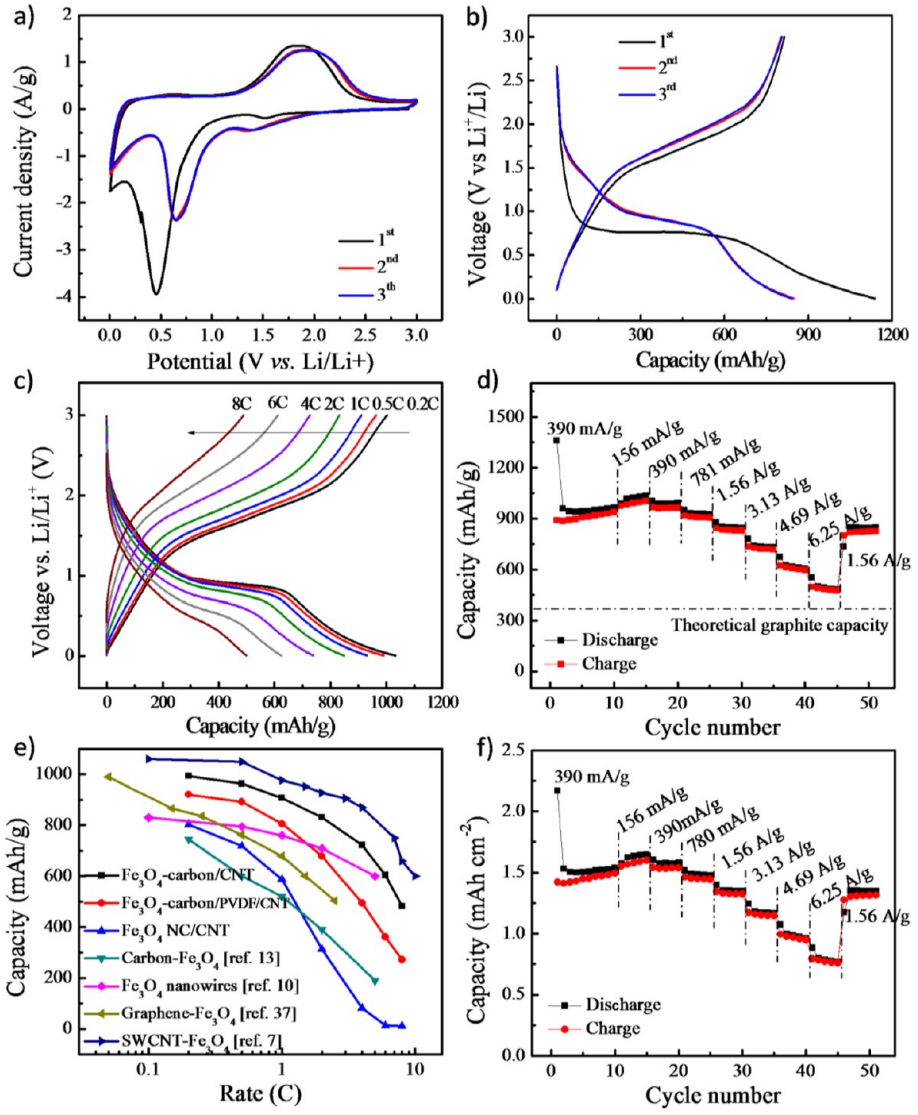

Figure 3. (a) Representative CV curves of an electrode based on the Fe_3O_4/carbon composite particles and CNTs obtained at a voltage range of 0.005 to 3.0 V (*vs* Li/Li^+) and potential scan rate of 0.5 mV s^{-1}. (b) Charge/discharge curves of the electrode achieved at the current density of 400 mA g^{-1} at the first few cycles. (c) Charge/discharge curves and corresponding charge/discharge time at different rates (0.2−8 C, 1 C = 780 mA g^{-1}). (d) Rate capability of the electrode at different current densities (0.156−6.25 A g^{-1}). (e) Comparison of capacity at different rates for such composite electrodes with those of iron oxide anodes reported. (f) Areal-normalized capacity of the composite electrode at different current densities calculated based on electrode area and mass loading.

than most iron-oxide-based electrodes reported (*e.g.*, carbon-coated Fe_3O_4 nanospindles,[13] nanowires,[10] graphene-wrapped Fe_3O_4,[37] and CNT-supported α-Fe_2O_3[12] anodes) and is comparable to that of thin single-walled CNT Fe_3O_4 electrodes.[7] Figure 3f shows that such composite electrodes present a footprint capacity up to 1.6 mAh cm^{-2}, which is close to those of graphite electrodes used in the commercial Li-ion batteries. Even at a current density of 1.56A g^{-1} (2 C), the electrodes can still deliver a footprint capacity of 1.3 mAh cm^{-2}, further implying the great potentials for real device applications.

Besides the high capacity and excellent rate capability, these composite electrodes also show excellent cycling stability, as displayed in Figure 4a. For example, the composite electrodes (thickness of *ca.* 50 μm) provide a capacity of 840 mAh g^{-1}at 390 mA g^{-1} without noticeable capacity loss during 100 cycles. Even at high current density (1.56 A g^{-1}), the electrodes still possess high capacity and good stability (Figure S4). In contrast, control electrodes fabricated by directly mixing Fe_3O_4 NCs with CNTs showed significantly lower stability (Figure S5), which demonstrates the advantages of using the aerosol-synthesized Fe_3O_4/carbon composite spheres for lithium storage. As for the traditional electrode using PVDF as binder, though it shows much stable capacity before 60 cycles, the stability cannot be maintained up to 100 cycles as the CNT-based composite electrodes. Those results further imply that the Fe_3O_4/carbon composite architecture together with

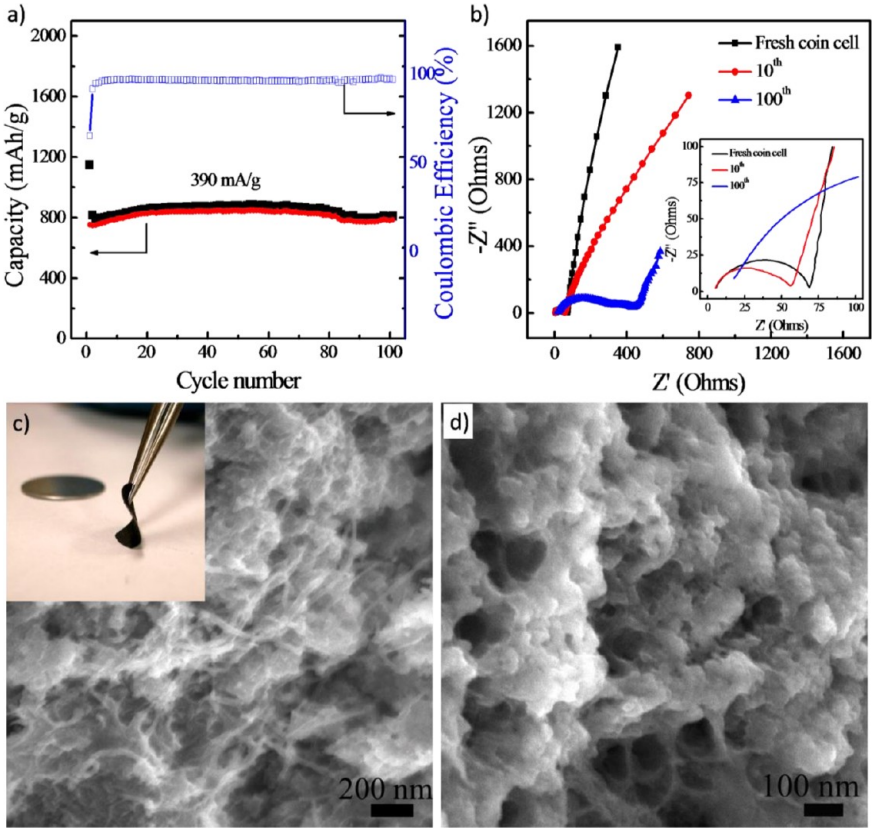

Figure 4. (a) Cycling stability of the composite electrode at a rate of 390 mA g^{-1}. (b) Electrochemical impedance spectra of the electrode at fresh coin cell, 10th and 100th discharge/charge cycles over the frequency range from 100 kHz to 0.01 Hz. Inset shows enlarged spectra at high-frequency range. (c,d) Morphology of the composite electrode after cycling, suggesting the formation of an SEI layer. Inset is the digital photograph of the electrode after 100 cycles showing electrodes with outstanding structure stability.

the CNT scaffold does significantly improve the electrical conductivity and mitigate mechanical stress generated during the charge/discharge process, which results in better active material utilization and cycling stability.

To further understand the structure and interfacial behavior of the composite electrodes during the cycling process, electrochemical impedance spectroscopy (EIS) was conducted along with different charge/discharge cycles at frequencies from 100 kHz to 0.01 Hz (Figure 4b). The Nyquist plots at different cycles (fresh electrode, after 10 cycles and after 100 cycles) show similar intercepts (around 4.5 Ω) with the real impedance axis (Z' axis). This resistance represents ohmic resistance from the contact, electrode, and resistance from electrolyte.[38,39] With frequency decreases, the electrode exhibits a semicircle due to the charge transfer resistance between the electrode and electrolyte. The fresh electrode showed a small diameter of the semicircle, which suggests that the composite electrodes possess smaller charge transfer resistance. There was a slight decrease in semicircle diameter after 10 cycles, indicating the good electrode stability with an activation process. The diameter of the semicircle increased in the following cycles, and after 100 cycles, the charge transfer resistance increased from 80 to 400 Ω, which is associated with forming SEI. The electrodes, however, still retained high capacities after cycling (Figure 4a), which indicates that the electron conduction and ion diffusion pathways in the robust electrode architecture were not affected by forming SEI during cycling. This property has been seldom achieved using traditional electrode structure for transition metal oxide anodes.

The following sloping region after the semicircle in the low-frequency region reflects the diffusion resistance of the electrolyte ions into the electrode. Due to the SEI layer formation, the slope decreased at the low-frequency region after 10 cycles, indicating an increased diffusion resistance. However, the slope showed a similar feature to the original electrode after 100 cycles, indicating that facile lithium diffusion channels can be produced during the reversible insertion/extraction process. After the cycling test, the whole film electrode maintained its integrity and flexibility (inset in Figure 4c). The structure and morphology of the cycled electrodes were further examined by SEM (Figure 4c,d). It reveals that the composite spheres retained their structure, suggesting the robustness of the spherical structure. A polymer/gel-like coating that can be ascribed to SEI

formation[37] surrounds the CNT networks and the composite particles. The nanocrystal clusters were still strongly linked and formed a porous structure with CNT scaffolds, which retained the structure integrity. Although the resistance may be increased slightly, the continuous CNT network and porous structure were still preserved, ensuring sufficient electronic and ion transport. This result suggests that the as-formed architecture is highly robust during cycling, ensuring their excellent electrochemical performance.

CONCLUSIONS

In summary, we have successfully demonstrated an effective fabrication of porous Fe_3O_4/carbon composite particles, where networks of Fe_3O_4 NCs were coated with continuous carbon layers. Intimately entangling the composite particles with CNT networks results in the formation of binder-free, mechanically robust, and high-performance lithium-ion anodes. Considering that iron oxide is cost-effective and large-scale production of CNTs has been realized,[40] such materials hold great potential for real applications. This effective strategy can be easily expanded to construct other high-performance architectures of CNTs and other metal oxides, providing a general and effective approach toward high-performance metal-oxide-based anodes.

METHODS

Synthesis of Fe_3O_4–Carbon Composite Particles. The Fe_3O_4 nanocrystals were synthesized through a co-precipitation method.[24] Typically, $FeCl_3$ (1.82 g) and $FeCl_2 \cdot 4H_2O$ (1.11 g) were dissolved in 150 mL of H_2O in a three-neck flask at 50 °C. Then 12 mL of 28 wt % aqueous ammonia solution was added into the flask to form Fe_3O_4 nanocrystals (NCs) by co-precipitation. Then, 1.6 g of P123 ($EO_{20}PO_{70}EO_{20}$, where EO and PO are ethylene oxide and propylene oxide, respectively) and 1.2 g of sucrose were added into the solution. The solution was sent through an atomizer using nitrogen as a carrier gas, as shown in Scheme 1A.[24] The aerosol droplets passed through a glass tube heated at 450 °C; as-formed particles were collected using a filter. Then, the particles were further annealed at 560 °C for 2 h under nitrogen to form the Fe_3O_4/carbon composite particles (Scheme 1B).

Fabrication of Film Electrodes. A vacuum filtration method was used to fabricate the electrodes with controllable thickness. First, aligned CNTs (produced by catalytic CVD growth[41]) were purified using HNO_3 and then dried for further use. The purified CNTs were then dispersed in *N*-methyl-2-pyrrolidone (NMP) to form 1 mg mL^{-1} solution. Ten milliliters of this CNT solution was mixed with 54.5 mg of the Fe_3O_4/carbon composite particles; free-standing composite films were formed by a vacuum filtration technique. For the control electrodes, as-synthesized Fe_3O_4 NCs were dried using a freeze-drying technique. Then, 32 mg of Fe_3O_4 NCs, 8.0 mg of CNTs, and 0.36 g of sucrose were dispersed in *N*,*N*-dimethylacetamide (DMAc). This solution was subjected to an identical filtration process to obtain free-standing films which were then annealed at 560 °C for 2 h. To make a traditional composite electrode, 77.5 wt % aerosol-synthesized Fe_3O_4/carbon composite particles, 12.5 wt % CNTs, and 10 wt % PVDF were mixed with NMP to form slurries. The homogeneous slurries were coated on steel substrates and dried under vacuum at 100 °C for another 12 h. The mass loading was ~1.5 mg cm^{-2} on each current collector.

Material Characterizations. X-ray diffraction (XRD) was conducted on a Panalytical X'Pert Pro X-ray powder diffractometer using Cu Kα radiation (λ = 1.54 Å). Nitrogen sorption isotherms were measured at 77 K with a Micromeritics ASAP 2020 analyzer. The specific surface areas (S_{BET}) were calculated by the Brunauer–Emmett–Teller (BET) method using adsorption branch in a relative pressure range from 0.04 to 0.25. The pore size distributions (D_p) were derived from the adsorption branch of isotherms using the Barrett–Joyner–Halenda (BJH) model. Thermogravimetric analysis (TGA) was conducted on a TGA Q50 instrument at a ramping rate of 10 °C min^{-1} under an air flow. SEM experiments were conducted on a JEOL JSM-6700 FE-SEM. TEM experiments were conducted on a FEI T12 instrument operated at 120 kV. The electrode films were cut into sheets for mechanical tests, which were conducted on an INSTRON 5564 with a speed of 2.0 mm min^{-1} at room temperature.

For electrochemical test, the electrodes were assembled into 2032-type coin cells. The electrolyte solution was 1.0 M $LiPF_6$ in ethylene carbonate (EC)/diethyl carbonate (DEC) (1:1 by volume), and lithium foils were used as both the counter and reference electrodes. The CV and EIS measurements were carried out on a Solartron 1860/1287 electrochemical interface. Coin cell assemblies were conducted in an argon-filled glovebox. The galvanostaic charge/discharge measurements were carried out by LAND CT2000 battery tester at different rates.

Conflict of Interest: The authors declare no competing financial interest.

Acknowledgment. This work was partially supported by the China National Program (2011CB932602) (F.W.) and was supported as part of the Molecularly Engineered Energy Materials, an Energy Frontier Research Center funded by the U.S. Department of Energy, Office of Science, Office of Basic Energy Sciences under Award DE-SC001342 (Y.L.). The authors acknowledge the support from General Motor Inc. and IMRA America Inc. The authors would also like to thank Celgard LLC for kind donation of battery separator (Celgard 2500).

Supporting Information Available: Supplementary TEM, TGA, and galvanostatic charge/discharge data are included. This material is available free of charge *via* the Internet at http://pubs.acs.org.

REFERENCES AND NOTES

1. Arico, A. S.; Bruce, P.; Scrosati, B.; Tarascon, J.-M.; van Schalkwijk, W. Nanostructured Materials for Advanced Energy Conversion and Storage Devices. *Nat. Mater.* **2005**, *4*, 366–377.
2. Karden, E.; Ploumen, S.; Fricke, B.; Miller, T.; Snyder, K. Energy Storage Devices for Future Hybrid Electric Vehicles. *J. Power Sources* **2007**, *168*, 2–11.
3. Scrosati, B.; Garche, J. Lithium Batteries: Status, Prospects and Future. *J. Power Sources* **2010**, *195*, 2419–2430.
4. Bruce, P. G.; Scrosati, B.; Tarascon, J.-M. Nanomaterials for Rechargeable Lithium Batteries. *Angew. Chem., Int. Ed.* **2008**, *47*, 2930–2946.
5. Liu, C.; Li, F.; Ma, L. P.; Cheng, H. M. Advanced Materials for Energy Storage. *Adv. Mater.* **2010**, *22*, E28–E62.
6. Poizot, P.; Laruelle, S.; Grugeon, S.; Dupont, L.; Tarascon, J. M. Nano-Sized Transition-Metal Oxides as Negative-Electrode Materials for Lithium-Ion Batteries. *Nature* **2000**, *407*, 496–499.
7. Ban, C.; Wu, Z.; Gillaspie, D. T.; Chen, L.; Yan, Y.; Blackburn, J. L.; Dillon, A. C. Nanostructured Fe_3O_4/SWNT Electrode: Binder-Free and High-Rate Li-Ion Anode. *Adv. Mater.* **2010**, *22*, E145–E149.
8. Cui, Z. M.; Jiang, L. Y.; Song, W. G.; Guo, Y. G. High-Yield Gas–Liquid Interfacial Synthesis of Highly Dispersed

Fe_3O_4 Nanocrystals and Their Application in Lithium-Ion Batteries. *Chem. Mater.* **2009**, *21*, 1162–1166.
9. Wang, L.; Yu, Y.; Chen, P. C.; Zhang, D. W.; Chen, C. H. Electrospinning Synthesis of C/Fe_3O_4 Composite Nanofibers and Their Application for High Performance Lithium-Ion Batteries. *J. Power Sources* **2008**, *183*, 717–723.
10. Muraliganth, T.; Vadivel Murugan, A.; Manthiram, A. Facile Synthesis of Carbon-Decorated Single-Crystalline Fe_3O_4 Nanowires and Their Application as High Performance Anode in Lithium Ion Batteries. *Chem. Commun.* **2009**, 7360–7362.
11. Yoon, T.; Chae, C.; Sun, Y.-K.; Zhao, X.; Kung, H. H.; Lee, J. K. Bottom-Up *In Situ* Formation of Fe_3O_4 Nanocrystals in a Porous Carbon Foam for Lithium-Ion Battery Anodes. *J. Mater. Chem.* **2011**, *21*, 17325–17330.
12. Wang, Z.; Luan, D.; Madhavi, S.; Hu, Y.; Lou, X. W. Assembling Carbon-Coated α-Fe_2O_3 Hollow Nanohorns on the CNT Backbone for Superior Lithium Storage Capability. *Energy Environ. Sci.* **2012**, *5*, 5252–5256.
13. Zhang, W. M.; Wu, X. L.; Hu, J. S.; Guo, Y. G.; Wan, L. J. Carbon Coated Fe_3O_4 Nanospindles as a Superior Anode Material for Lithium-Ion Batteries. *Adv. Funct. Mater.* **2008**, *18*, 3941–3946.
14. Kang, B.; Ceder, G. Battery Materials for Ultrafast Charging and Discharging. *Nature* **2009**, *458*, 190–193.
15. Guo, B.; Wang, X; Fulvio, P. F; Chi, M.; Mahurin, S. M.; Sun, X.-G.; Dai, S. Soft-Templated Mesoporous Carbon-Carbon Nanotube Composites for High Performance Lithium-Ion Batteries. *Adv. Mater.* **2011**, *23*, 4661–4666.
16. Landi, B. J.; Ganter, M. J.; Cress, C. D.; DiLeo, R. A.; Raffaelle, R. P. Carbon Nanotubes for Lithium Ion Batteries. *Energy Environ. Sci.* **2009**, *2*, 638–654.
17. Wu, Z. S.; Zhou, G.; Yin, L. C.; Ren, W.; Li, F.; Cheng, H. M. Graphene/Metal Oxide Composite Electrode Materials for Energy Storage. *Nano Energy* **2012**, *1*, 107–131.
18. Paek, S.-M.; Yoo, E.; Honma, I. Enhanced Cyclic Performance and Lithium Storage Capacity of SnO_2/Graphene Nanoporous Electrodes with Three-Dimensionally Delaminated Flexible Structure. *Nano Lett.* **2009**, *9*, 72–75.
19. Wang, D.; Kou, R.; Choi, D.; Yang, Z.; Nie, Z.; Li, J.; Saraf, L. V.; Hu, D.; Zhang, J.; Graff, G. L.; Liu, J.; Pope, M. A.; Aksay, I. A. Ternary Self-Assembly of Ordered Metal Oxide–Graphene Nanocomposites for Electrochemical Energy Storage. *ACS Nano* **2010**, *4*, 1587–1595.
20. Magasinski, A.; Dixon, P.; Hertzberg, B.; Kvit, A.; Ayala, J.; Yushin, G. High-Performance Lithium-Ion Anodes Using a Hierarchical Bottom-Up Approach. *Nat. Mater.* **2010**, *9*, 353–358.
21. Jung, Y. S.; Cavanagh, A. S.; Riley, L. A.; Kang, S.-H.; Dillon, A. C.; Groner, M. D.; George, S. M.; Lee, S.-H. Ultrathin Direct Atomic Layer Deposition on Composite Electrodes for Highly Durable and Safe Li-Ion Batteries. *Adv. Mater.* **2010**, *22*, 2172–2176.
22. Scott, I. D.; Jung, Y. S.; Cavanagh, A. S.; Yan, Y.; Dillon, A. C.; George, S. M.; Lee, S.-H. Ultrathin Coatings on Nano-$LiCoO_2$ for Li-Ion Vehicular Applications. *Nano Lett.* **2011**, *11*, 414–418.
23. Zhu, T.; Chen, J. S.; Lou, X. W. Glucose-Assisted One-Pot Synthesis of FeOOH Nanorods and Their Transformation to Fe_3O_4@Carbon Nanorods for Application in Lithium Ion Batteries. *J. Phys. Chem. C* **2011**, *115*, 9814–9820.
24. Lu, Y.; Fan, H.; Stump, A.; Ward, T. L.; Rieker, T.; Brinker, C. J. Aerosol-Assisted Self-Assembly of Mesostructured Spherical Nanoparticles. *Nature* **1999**, *398*, 223–226.
25. Boissiere, C.; Grosso, D.; Chaumonnot, A.; Nicole, L.; Sanchez, C. Aerosol Route to Functional Nanostructured Inorganic and Hybrid Porous Materials. *Adv. Mater.* **2011**, *23*, 599–623.
26. Jia, X.; Yan, C.; Chen, Z.; Wang, R.; Zhang, Q.; Guo, L.; Wei, F.; Lu, Y. Direct Growth of Flexible $LiMn_2O_4$/CNT Lithium-Ion Cathodes. *Chem. Commun.* **2011**, *47*, 9669–9671.
27. Xu, G.; Zheng, C.; Zhang, Q.; Huang, J.; Zhao, M.; Nie, J.; Wang, X.; Wei, F. Binder-Free Activated Carbon/Carbon Nanotube Paper Electrodes for Use in Supercapacitors. *Nano Res.* **2011**, *4*, 870–881.
28. Ogihara, T.; Kodera, T.; Myoujin, K.; Motohira, S. Preparation and Electrochemical Properties of Cathode Materials for Lithium Ion Battery by Aerosol Process. *Mater. Sci. Eng., B* **2009**, *161*, 109–114.
29. Guo, J.; Liu, Q.; Wang, C.; Zachariah, M. R. Interdispersed Amorphous MnO_x–Carbon Nanocomposites with Superior Electrochemical Performance as Lithium-Storage Material. *Adv. Funct. Mater.* **2012**, *22*, 803–811.
30. Zhang, Q.; Huang, J. Q.; Zhao, M. Q.; Qian, W. Z.; Wei, F. Carbon Nanotube Mass Production: Principles and Processes. *ChemSusChem* **2011**, *4*, 864–889.
31. Chen, X.; Li, L.; Sun, X.; Liu, Y.; Luo, B.; Wang, C.; Bao, Y.; Xu, H.; Peng, H. Magnetochromatic Polydiacetylene by Incorporation of Fe_3O_4 Nanoparticles. *Angew. Chem., Int. Ed.* **2011**, *50*, 5486–5489.
32. Luo, S.; Wang, K.; Wang, J.; Jiang, K.; Li, Q.; Fan, S. Binder-Free $LiCoO_2$/Carbon Nanotube Cathodes for High-Performance Lithium Ion Batteries. *Adv. Mater.* **2012**, *24*, 2294–2298.
33. Chen, Z.; Zhang, D.; Wang, X.; Jia, X.; Wei, F.; Li, H.; Lu, Y. High-Performance Energy-Storage Architectures from Carbon Nanotubes and Nanocrystal Building Blocks. *Adv. Mater.* **2012**, *24*, 2030–2036.
34. Zhu, X.; Zhu, Y.; Murali, S.; Stoller, M. D.; Ruoff, R. S. Nanostructured Reduced Graphene Oxide/Fe_2O_3 Composite as a High-Performance Anode Material for Lithium Ion Batteries. *ACS Nano* **2011**, *5*, 3333–3338.
35. Yuan, S. M.; Li, J. X.; Yang, L. T.; Su, L. W.; Liu, L.; Zhou, Z. Preparation and Lithium Storage Performances of Mesoporous Fe_3O_4@C Microcapsules. *ACS Appl. Mater. Interfaces* **2011**, *3*, 705–709.
36. Taberna, P. L.; Mitra, S.; Poizot, P.; Simon, P.; Tarascon, J. M. High Rate Capabilities Fe_3O_4-Based Cu Nano-Architectured Electrodes for Lithium-Ion Battery Applications. *Nat. Mater.* **2006**, *5*, 567–573.
37. Zhou, G.; Wang, D. W.; Li, F.; Zhang, L.; Li, N.; Wu, Z. S.; Wen, L.; Lu, G. Q.; Cheng, H. M. Graphene-Wrapped Fe_3O_4 Anode Material with Improved Reversible Capacity and Cyclic Stability for Lithium Ion Batteries. *Chem. Mater.* **2010**, *22*, 5306–5313.
38. Largeot, C.; Portet, C.; Chmiola, J.; Taberna, P.-L.; Gogotsi, Y.; Simon, P. Relation between the Ion Size and Pore Size for an Electric Double-Layer Capacitor. *J. Am. Chem. Soc.* **2008**, *130*, 2730–2731.
39. Kou, Y.; Xu, Y.; Guo, Z.; Jiang, D. Supercapacitive Energy Storage and Electric Power Supply Using an Aza-Fused π-Conjugated Microporous Framework. *Angew. Chem., Int. Ed.* **2011**, *50*, 8753–8757.
40. Wei, F.; Zhang, Q.; Qian, W. Z.; Yu, H.; Wang, Y.; Luo, G. H.; Xu, G. H.; Wang, D. Z. The Mass Production of Carbon Nanotubes Using a Nano-agglomerate Fluidized Bed Reactor: A Multiscale Sapce-Time Analysis. *Powder Technol.* **2008**, *183*, 10–20.
41. Zhang, Q.; Zhao, M. Q.; Tang, D. M.; Li, F.; Huang, J. Q.; Liu, B.; Zhu, W. C.; Zhang, Y. H.; Wei, F. Carbon-Nanotube-Array Double Helices. *Angew. Chem., Int. Ed.* **2010**, *49*, 3642–3645.